INTERNATIONAL JOURNAL FOR NUMERICAL METHODS IN FLUIDS
Int. J. Numer. Meth. Fluids 2003; **42**:1293–1319 (DOI: 10.1002/fld.585)

Evaluation of one- and two-equation low-*Re* turbulence models. Part I—Axisymmetric separating and swirling flows

M. I. Yaras*,†,‡ and A. D. Grosvenor§

Department of Mechanical and Aerospace Engineering, Carleton University, Ottawa, Ont., Canada K1S 5B6

SUMMARY

This first segment of the two-part paper systematically examines several turbulence models in the context of three flows, namely a simple flat-plate turbulent boundary layer, an axisymmetric separating flow, and a swirling flow. The test cases are chosen on the basis of availability of high-quality and detailed experimental data. The tested turbulence models are integrated to solid surfaces and consist of: Rodi's two-layer k–ε model, Chien's low-Reynolds number k–ε model, Wilcox's k–ω model, Menter's two-equation shear-stress-transport model, and the one-equation model of Spalart and Allmaras. The objective of the study is to establish the prediction accuracy of these turbulence models with respect to axisymmetric separating flows, and flows of high streamline curvature. At the same time, the study establishes the minimum spatial resolution requirements for each of these turbulence closures, and identifies the proper low-Mach-number preconditioning and artificial diffusion settings of a Reynolds-averaged Navier–Stokes algorithm for optimum rate of convergence and minimum adverse impact on prediction accuracy. Copyright © 2003 John Wiley & Sons, Ltd.

KEY WORDS: low-Re turbulence modelling; axisymmetric separation; swirling flows

1. INTRODUCTION

Turbulence closures based on one or two partial differential transport equations exist in virtually every commercial general-purpose computational fluid dynamics (CFD) code today. These models are built on the eddy-viscosity hypothesis, and as such lack representation of turbulence anisotropy and Reynolds-stress relaxation in response to sudden changes in the strain field. Despite these shortcomings, however, in most instances they are still preferred over higher-order Reynolds stress closures due to their substantially lower computational overhead. Initially, these eddy-viscosity models relied on wall functions for boundary conditions at solid surfaces. These functions are based on the assumption of local equilibrium

* Correspondence to: M.I. Yaras, Department of Mechanical and Aerospace Engineering, Carleton University, 1125 Colonel By Drive, Ottawa, Ontario, Canada KlS 5B6.
† E-mail: Metin_Yaras@carieton.ca
‡ Associate Professor.
§ Graduate Student.

Contract/grant sponsor: National Research Council of Canada; contract/grant number: 31184-8-8847/001/ST

Received 3 November 2000
Revised 21 April 2003

of turbulence, i.e. they assume the existence of a balance between the production and dissipation rates of turbulence. This assumption is often not valid, such as in unsteady flows, in separated boundary layers, or in instances where strong secondary flows penetrate into the viscous sublayer [1]. Significant increases in computational power over the last decade has made more refined resolution of the boundary layer practical. This, in turn, has allowed integration of the turbulence transport equations to solid surfaces, circumventing the restrictions brought about by the wall-function approach. Numerous 'low Reynolds number' turbulence models have been developed that facilitate this process of integration to solid surfaces [2, 3]. It has been suggested that as many as 60–100 nodes are needed across a boundary layer for proper numerical resolution with such turbulence models [4]. As more and more of these models are incorporated into mainstream computational tools, it is important that systematic studies be undertaken to establish their accuracy and minimum spatial-resolution requirements.

Five such turbulence models have been evaluated in the present study for prediction accuracy, numerical robustness and computational efficiency based on test cases ranging from a two-dimensional equilibrium boundary layer to separated and swirling flows. These turbulence models consists of: the low-Re k–ε model of Chien [5], the two-layer k–ε model of Rodi and his co-workers [6], the k–ω model of Wilcox [7], the two-equation shear-stress-transport model of Menter [8], and the one-equation eddy-viscosity model of Spalart and Allmaras [9]. The simulations contained in this study are presented in the order of increasing flow complexity. The first flow consists of an equilibrium flat-plate turbulent boundary layer performed as a baseline test case. The second test case is based on an axisymmetric annular diffusing flow allowing evaluation of the turbulence models with respect to behaviour under adverse streamwise pressure gradient and separated conditions. The third case involves an axisymmetric swirling flow and establishes the predictive accuracy of the turbulence models under the effects of strong streamwise curvature. These test cases are then followed by significantly more complex, three-dimensional flows associated with a vortex-generator jet and a diffusing S-duct, presented in Part II of this study.

2. NUMERICAL TECHNIQUE

2.1. Algorithm

A general-purpose Navier–Stokes solver developed by the first author of this work has been used in the simulations. The algorithm is based on the solution of the Navier–Stokes equations expressed in integral, strong-conservation-law form:

$$\int_{\vartheta} (Q_t + E_x + F_y + G_z)\, \mathrm{d}\vartheta = 0 \tag{1}$$

where the subscripts indicate derivatives and,

$$Q = \begin{pmatrix} \rho \\ \rho V_x \\ \rho V_y \\ \rho V_z \end{pmatrix}, \quad E = \begin{pmatrix} \rho V_x \\ \rho V_x^2 + p - \tau_{xx} \\ \rho V_x V_y - \tau_{xy} \\ \rho V_x V_z - \tau_{xz} \end{pmatrix}, \quad F = \begin{pmatrix} \rho V_y \\ \rho V_x V_y - \tau_{yx} \\ \rho V_y^2 + p - \tau_{yy} \\ \rho V_y V_z - \tau_{yz} \end{pmatrix}, \quad G = \begin{pmatrix} \rho V_z \\ \rho V_x V_z - \tau_{zx} \\ \rho V_y V_z - \tau_{zy} \\ \rho V_z^2 + p - \tau_{zz} \end{pmatrix} \tag{2}$$

with

$$\tau_{xx} = \frac{2}{3}\rho(\nu + \nu_e)\left(2\frac{\partial V_x}{\partial x} - \frac{\partial V_y}{\partial y} - \frac{\partial V_z}{\partial z}\right), \quad \tau_{xy} = \rho(\nu + \nu_e)\left(\frac{\partial V_x}{\partial y} + \frac{\partial V_y}{\partial x}\right) \tag{3}$$

and similarly for the remaining normal and shear stresses.

Although the algorithm has been developed for the prediction of both incompressible and compressible flows, the present description is given for incompressible flows in keeping with the nature of the present simulations. Discretization in space is based on a vertex-centred finite-volume scheme using a structured grid of quadrilateral (hexahedral in three-dimensional space) cells [10]. In this approach, the conserved variables are stored at the vertices of the grid cells, and the faces of the control volume associated with a vertex are formed by connecting the centroids of the quadrilaterals surrounding the vertex to the midpoints of the edges passing through the vertex. Both convective and diffusive fluxes are calculated at the vertices and are interpolated to the control-volume faces. The spatial gradients appearing in the diffusive fluxes at a vertex are obtained by applying Gauss' divergence theorem to the control volume surrounding the vertex.

On a uniform grid, the interpolation of the flux terms outlined above is equivalent to centred differencing, yielding second-order discretization accuracy. Except for very low grid-cell Reynolds numbers, such treatment of convective fluxes is well-known to cause instability and requires inclusion of an artificial dissipation term into the governing equations. This artificial dissipation term, $D(Q)$, is traditionally constructed from second- and fourth-order differences of the conservation variables in all grid directions [11], i.e.

$$\int_{\vartheta} (Q_t + E_x + F_y + G_z)\,\mathrm{d}\vartheta - (D_\xi^{(2)} - D_\xi^{(4)} + D_\eta^{(2)} - D_\eta^{(4)} + D_\zeta^{(2)} - D_\zeta^{(4)})Q = 0 \tag{4}$$

where subscripts ξ, η, ζ denote the three grid directions of the structured grid. For instance considering the ξ direction,

$$D_\xi^{(2)}Q = \nabla_\xi((\lambda_\xi)_{i-1/2,j,k}(\varepsilon_\xi)^{(2)}_{i-1/2,j,k})\Delta_\xi Q_{i,j,k} \tag{5}$$

$$D_\xi^{(4)}Q = \nabla_\xi((\lambda_\xi)_{i-1/2,j,k}(\varepsilon_\xi)^{(4)}_{i-1/2,j,k})\Delta_\xi\nabla_\xi\Delta_\xi Q_{i,j,k} \tag{6}$$

where i, j, k denote indices in the ξ, η, ζ grid directions, λ is the spectral radius of the inviscid-flux Jacobian, and ∇_ξ, Δ_ξ are first-order forward and backward differencing operators in the ξ grid direction. These operators need to be modified at computational domain boundaries, and the approach recommended by Swanson and Turkel [12] is adopted in the present algorithm. $\varepsilon^{(2)}$ and $\varepsilon^{(4)}$ are scaling parameters for the dissipation terms. $\varepsilon^{(2)}$ is assigned values such that the $D^{(2)}$ term is activated only in regions of high pressure gradients:

$$(\varepsilon_\xi)^{(2)}_{i-1/2,j,k}) = \kappa^{(2)}\ \max((\varphi_\xi)_{i-1,j,k}, (\varphi_\xi)_{i,j,k}) \tag{7}$$

$$(\varphi_\xi)_{i,j,k} = \left|\frac{\Delta_\xi\nabla_\xi p_{i,j,k}}{(4 + \Delta_\xi\nabla_\xi)p_{i,j,k}}\right|, \quad \kappa^{(2)} = 0.25 \tag{8}$$

and $\varepsilon^{(4)}$ is quantified using

$$(\varepsilon_\xi)^{(4)}_{i-1/2,j,k} = \max(0, \kappa^{(4)} - (\varepsilon_\xi)^{(2)}_{i-1/2,j,k}), \quad \kappa^{(4)} = \text{const.} \tag{9}$$

In absence of high pressure gradients, only the third-order accurate $D^{(4)}$ term is activated, allowing the second order formal accuracy of the spatial discretization to be retained. Due to low levels of local pressure gradients in the simulations presented herein, only the $D^{(4)}$ term influenced the solution. The minimum value of $\kappa^{(4)}$ that allowed stable convergence will be presented in later sections as part of the discussions of the test cases.

The spectral radii of the inviscid flux Jacobian matrices are the common scaling parameters for the artificial dissipation terms. Matrix valued scaling [13] results in less artificial diffusion entering into the numerical solution, albeit at the expense of reduced convergence rates [14]. In the present algorithm the scalar method of scaling is chosen. For example, the $(\lambda_\xi)_{i-1/2,j,k}$ component is obtained from

$$(\lambda_\xi)_{i-1/2,j,k} = (|V_\xi S_\xi| + ((c/a_1)^2 + V_\xi^2)^{1/2}|S_\xi|)_{i-1/2,j,k} \tag{10}$$

where S_ξ is the control volume surface facing the ξ grid direction, and c/a_1 is a preconditioning parameter, to be described later.

Discretization of the temporal derivative, Q_t, appearing in Equation (1) is based on three-point backward differencing, yielding second-order accuracy in time. An exception is the first time increment which is based on a two-point scheme. At each real-time increment, the discretized governing equations are then solved iteratively using pseudo-time stepping for relaxation:

$$(Q_{t_p}\vartheta)_{i,j,k} + \int_{\vartheta_{i,j,k}} (Q_t + E_x + F_y + G_z)\,\mathrm{d}\vartheta - D(Q_{i,j,k}) = 0 \tag{11}$$

For the steady-flow simulations presented herein, the temporal derivative, Q_t, was not involved in the computations. The vector of conservation variables, Q, used in the pseudo-time derivative, Q_{t_p}, is preconditioned to extend the range of applicability of the algorithm to low Mach-number flows.

The following form of preconditioning has been adopted which is similar to the one proposed by Turkel [15]:

$$\frac{\partial Q}{\partial t_p} = \begin{pmatrix} \left(\dfrac{a_1}{c}\right)^2 \dfrac{\partial p}{\partial t_p} \\ \left(\dfrac{a_2}{c}\right)^2 V_x \dfrac{\partial p}{\partial t_p} + \dfrac{\partial(\rho V_x)}{\partial t_p} \\ \left(\dfrac{a_3}{c}\right)^2 V_y \dfrac{\partial p}{\partial t_p} + \dfrac{\partial(\rho V_y)}{\partial t_p} \\ \left(\dfrac{a_4}{c}\right)^2 V_z \dfrac{\partial p}{\partial t_p} + \dfrac{\partial(\rho V_z)}{\partial t_p} \end{pmatrix} \tag{12}$$

where a_1, a_2, a_3, a_4 are constants, and c is a parameter which was scaled on the local flow velocity for the present simulations. The same value was assigned to the constants $a_{i=1,4}$. Variations were observed for the optimum value of this constant amongst the test cases considered.

The pseudo-time increments are adjusted locally to the maximum allowable value dictated by convective and diffusive numerical stability limitations:

$$\frac{1}{(\Delta t_p)_{i,j,k}} \geqslant \left(\frac{1}{\Delta t_c} + \frac{1}{\Delta t_d}\right)_{i,j,k} = \left(\frac{\Sigma\lambda}{K_c\vartheta} + \frac{1}{K_d\vartheta^2}\Sigma(\nu + \nu_e)S^2\right)_{i,j,k} \tag{13}$$

where the summations are performed over the surfaces of the control volume. The values for the constants K_c and K_d will be given later.

Marching in pseudo time is based on Runge–Kutta integration with explicit odd-numbered and implicit even-numbered stages. Such implicit treatment of alternate stages is analogous to the well-known implicit residual smoothing procedure [11] and enhances the stability margin of the algorithm over the purely explicit approach. A modified version of the Strongly-Implicit Procedure of Stone [16, 17] is used for the implicit stages. For computational efficiency, the artificial dissipation terms are evaluated only during the odd-numbered stages. For the simulations presented herein, two-stage Runge–Kutta integration was found to be sufficient to damp-out the high frequency pseudo-transients. The coefficients of both stages were set to 1.0.

Although the Runge–Kutta time integration process efficiently removes high-frequency errors during pseudo-time stepping, it is not efficient in dealing with errors of relatively large wave lengths. A multigrid scheme is used to deal with the longer wave lengths. The scheme is based on Full-Approximation-Storage [18] utilizing V cycles with conservative area-weighted interpolation during restriction and linear interpolation during prolongation. For the present simulations, two levels of grids with two coarse-grid time increments per cycle was found to provide the best trade-off between rate of reduction of residuals and increased computational effort due to the prolongation and restriction operations over each multigrid cycle. Due to reduced spatial resolution on the coarse grid, the physical and artificial diffusion terms were calculated on the fine-grid level only.

2.2. Turbulence models

The turbulence models evaluated in the present study are Rodi's two-layer k–ε model [6], Chien's low-Reynolds number k–ε model [5], Wilcox's k–ω model [7], Menter's two-equation shear-stress-transport model [8], and the one-equation model of Spalart and Allmaras [9]. These turbulence models were used in their standard configurations, with the various empirical constants set to values proposed by their respective developers [19]. As such, the models are not presented in detail here in the interest of brevity.

In the transport equations of turbulence, the discretization of the convective and diffusive terms, and the formulation of artificial dissipation is the same as for the mass and momentum conservation equations, described earlier. Point-implicit linearization of the source terms is utilized for enhanced stability. The resultant equations are solved with the remaining governing equations in a coupled fashion. Pre-conditioning of the pseudo-time derivative is not required for the turbulence equations, hence the constant a appearing in the pseudo-time derivative of the mass and momentum equations (see Equation (12)) is set to zero for the transport equations of turbulence. A curvature correction term, F_{cr}, is introduced to account for the effects of streamline curvature. The formulation of this term follows the recommendation of

Hellsten [20]:

$$F_{\mathrm{cr}} = \frac{1}{1 + C_{\mathrm{cr}} \dfrac{\Omega}{S}\left(\dfrac{\Omega}{S} - 1\right)} \tag{14}$$

where Ω is the magnitude of the local vorticity vector, S is a scalar measure of the local strain rate tensor ($= \sqrt{2S_{ij}S_{ij}}$), and C_{cr} is a constant. The F_{cr} term multiplies the production term of the eddy viscosity equation of the Spalart–Allmaras (SA) model, and the destruction term of the transport equation for the turbulence dissipation rate in the remaining turbulence models.

At wall boundaries, k, $\tilde{\varepsilon}$, $\mathrm{d}\varepsilon/\mathrm{d}n$ and $\tilde{\nu}_e$ are set to zero. In the SST turbulence model, the wall value of ω is determined using

$$\omega_{\mathrm{wall}} = \frac{6\beta_{\mathrm{wall}}\nu}{0.075\, y_1^2} \tag{15}$$

A value of $\beta_{\mathrm{wall}} = 10$ was given by Menter [8], whereas Hellsten [21] suggested 1.25. Sensitivity of the simulation results to the value of β_{wall} will be discussed in the context of flat-plate boundary layer simulations.

In the k–ω turbulence model, the wall value of ω is obtained from:

$$\omega_{\mathrm{wall}} = \frac{U_\tau^2 S_R}{\nu} \tag{16}$$

where

$$S_R = \begin{cases} (50/k_R^+)^2 & k_R^+ \leqslant 25 \\ 100/k_R^+ & k_R^+ > 25 \end{cases} \tag{17}$$

The parameter k_R^+ was calculated as per the recommendation of Hellsten [21] for smooth walls:

$$k_R^+ = 2.4\, y_1^{+^{0.85}} \tag{18}$$

3. SIMULATIONS OF A FLAT-PLATE BOUNDARY LAYER

The flat-plate turbulent boundary layer is expected to pose the least challenge to a turbulence model due to the equilibrium state of the turbulence. As such, the relatively complex turbulence models considered in this study are expected to perform well for this flow. The primary motivation for including this flow into the study was to establish the baseline performance of the models in question, and establish their sensitivity to spatial resolution, freestream turbulence settings and numerical diffusion.

3.1. Computational domain, boundary conditions and iteration parameters

The simulations were conducted with a computational domain of 0.15 m height, 2.1 m length, freestream velocity of 33 m/s, and a Reynolds number based on length (L) of 4.5×10^6.

A 0.1 m long 'slip wall' boundary was placed upstream of the plate leading edge. Both the upper and aft boundaries of the computational domain were set as outflow boundaries with a fixed, spatially uniform static pressure. All flow variables other than pressure were extrapolated to the outflow boundaries from within the computational domain. At the inflow boundary, uniform distributions of velocity, flow direction and turbulence properties were imposed and static pressure was extrapolated from the interior nodes.

The inflow turbulence properties were set to: $k = 1.3 \times 10^{-3}$, $\varepsilon = 7$ for the k–ε models of Rodi and Chien; $k = 1.8 \times 10^{-6}$, $\omega = 100$ for the k–ω and SST models and $\chi = 0.77$ for the SA model. The predictions were confirmed to be insensitive to small variations in these inflow settings of turbulence properties. The initial distributions of the turbulence parameters throughout the computational domain were matched to these values at the inflow boundary. Rodi's model was an exception to this, for it was observed that low initial values of k resulted in convergence towards laminar flow before arriving at the turbulent solution, which increased the required computing time. Use of an initial value of $k = 0.11$, corresponding to $\mu_e/\mu = 10$, avoided this particular transient path. During the course of pseudo-time marching to a steady state solution, it is plausible for the turbulence parameters to temporarily assume negative values. This nonphysical behavior would likely cause divergence of the solution. This problem was avoided by imposing lower limits on the turbulence parameters which, in the present case, were matched to the turbulence specifications at the inflow boundary. This choice of lower limits prevented decay of freestream turbulence with downstream distance, thereby providing homogeneous action of simulated freestream turbulence along the length of the boundary layer.

For optimum rates of convergence to a solution, the artificial compressibility parameter, c/a, was set to $\max[1.0\ \mathrm{m/s}; 1.4V_{\mathrm{local}}]$. Acceptable levels of convergence was feasible with values up to $\max[1.0\ \mathrm{m/s}; 2.2V_{\mathrm{local}}]$. Calculation of convective and diffusive pseudo-time-step limits were based on $K_c = 1.8$ and $K_d = 0.5$, and the artificial-diffusion parameter, κ_4, was set to 0.005.

3.2. Computational grid

The simulations were performed for several combinations of boundary layer cross-stream resolution and y_1^+ values to establish sensitivity to these parameters. The first grid consisted of 273 nodes in the streamwise direction with clustering towards the leading edge, and 129 nodes in the cross-stream direction with 82 of these nodes contained within the maximum boundary layer thickness of 0.04 m at the trailing edge of the plate. The node count within the boundary layer was determined on the basis of boundary layer edge location identified with an edge velocity that is 99% of the freestream value. The distance of the first node from the plate surface corresponded to $y_1^+ = 1.25$ at $x/L = 0.6$. This was the finest grid tested, and was chosen to suit the y_1^+ as well as boundary layer resolution requirements of all four models based on the information available in the literature [20, 22, 23]. Subsequent grids were reduced in resolution, and the distance of the first node from the wall was varied in an attempt to identify the coarsest grid with the largest y_1^+ that provided C_f values within 5% of the experimental data. The 5% threshold was chosen somewhat arbitrarily as a reasonable level of accuracy for C_f in engineering analysis. The streamwise number of nodes in these coarser grids was set to 97. Cross-stream resolution was reduced to 45 and 23 nodes, yielding 31 and 15 nodes, respectively, within the boundary layer thickness at the trailing edge of the

plate. The distance of the first node from the wall was varied within these two coarse grid resolutions. Values of approximately $y_1^+ = 3$ and 5 were obtained at $x/L = 0.6$.

3.3. Simulation results

In what follows, the predicted skin friction coefficient distribution and the velocity profile at $x/L = 0.6$ are compared with the data of Wieghardt and Tillmann [24], whereas the data compiled by Patel *et al.* [25] is used as a reference for the predicted k profile at the same streamwise position. The band of variation in the k data compiled by Patel *et al.* is as large as $\pm 25\%$. Thus, evaluation of the prediction accuracy for k is qualitative. The choice of $x/L = 0.6$ as the streamwise location for analysis of the results was arbitrary, and represents the trends observed at other streamwise positions.

Predicted streamwise distribution of C_f and profiles of streamwise velocity and turbulence kinetic energy at $x/L = 0.6$ are compared to experimental data in Figures 1–5. For the k–ω and SST turbulence models, the results are shown for two of the grids only, since the discrepancy between the predicted and experimental C_f data was well beyond the 5% threshold with the remaining grids. In the plots, symbols are included to correspond with node locations on the prediction curves to provide a visual impression of the boundary layer resolution. Rodi's k–ε model displays the least amount of dependence on boundary-layer resolution and y_1^+, and is closely followed by the SA model in this respect. Both models produce reasonably accurate results for the C_f and velocity distributions on the coarsest grid considered ($y_1^+ = 5$ at $x/L = 0.6$; 15 nodes in the boundary layer at $x/L = 1.0$). The SST and k–ω models, on the other hand, already yield prediction errors on the second finest grid ($y_1^+ = 2.8$ at $x/L = 0.6$; 31 nodes in the boundary layer at $x/L = 1.0$) that are somewhat greater than those with the k–ε and SA models on the coarsest grid. These results were used as guidelines in the construction of the grids in near-wall regions of the remaining test cases of this study. Convergence problems were encountered with Chien's k–ε model, caused by excessive amounts of production of turbulence energy at the leading edge. Rather than limiting the production of turbulence, simulations with this model were based on a computational domain with an inflow positioned downstream of the leading edge of the plate. The inflow boundary-layer profiles of mean-flow and turbulence properties were obtained from the simulations with Rodi's k–ε model. For convergence, it was necessary to adjust the lower limit of c/a from 1.0 to 15.0 m/s, and the value of K_d from 0.1 to 0.5. As shown in Figure 5, the prediction accuracy is comparable to those of other models. The C_f trend in close vicinity of the inflow boundary is the result of a slight error in polynomial representation of the inflow velocity profile very close to the plate surface. Interestingly, Chien's k–ε model is the only one that distinctly predicts the expected peak in k near the wall, albeit only qualitatively. Due to problems encountered with this model in the subsequent test flows, optimization of spatial resolution was not attempted for this model.

3.3.1. Sensitivity to artificial diffusion. In incompressible-flow simulations, the fourth-order artificial dissipation term, $D^{(4)}$, tends to be dominant since the pressure gradients are not large enough to produce noticeable magnitudes for the second-order term. The effect of this artificial dissipation term on the prediction accuracy was evaluated through simulations with two different values of the scaling coefficient κ_4 : 0.005 and 0.01. Differences were apparent only on the coarser of the tested grids. This dependence of artificial dissipation on grid

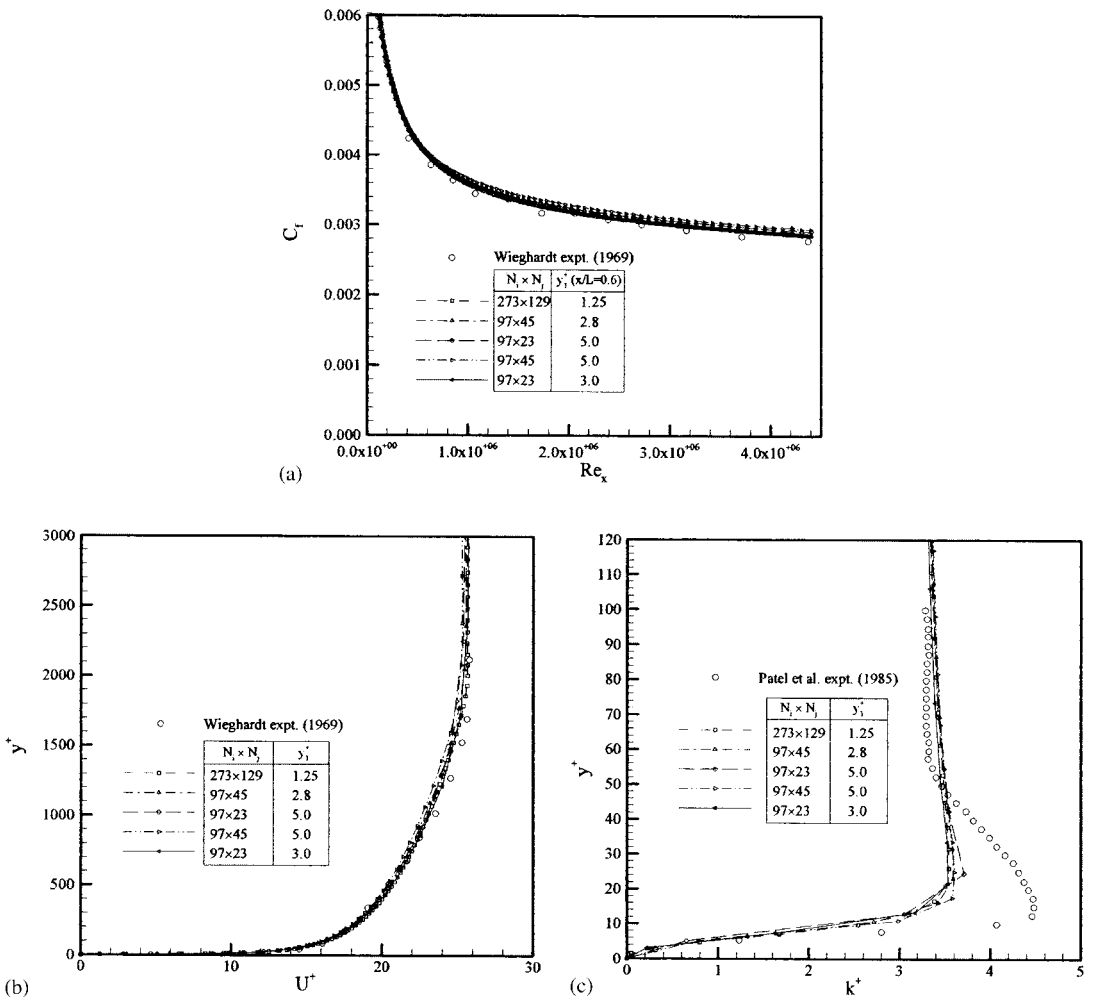

Figure 1. Flat-plate predictions based on Rodi's k–ε model—sensitivity to spatial resolution: (a) C_f distribution; (b) velocity profile at $(x/L = 0.6)$; and (c) k profile at $(x/L = 0.6)$.

resolution is expected since node spacings dictate the distances over which the fourth-order difference appearing in the artificial dissipation term is evaluated. Considering the close agreement between different grid resolutions in Figures 1–4 evaluated with $\kappa_4 = 0.005$, this κ_4 value is deemed sufficiently low to prevent numerical diffusion from overshadowing physical trends.

3.3.2. Sensitivity to wall boundary conditions. Implementation of wall boundary conditions for each of the turbulence models was described earlier. A key parameter in the calculation of ω_{wall} for the SST model is β_{wall}. A value of 10 was proposed for this parameter by Menter [8], whereas Hellsten [21] noted that an increase of β_{wall} above 1.25 tends to amplify the dependence of the SST model predictions on grid resolution. Present simulations indicated the

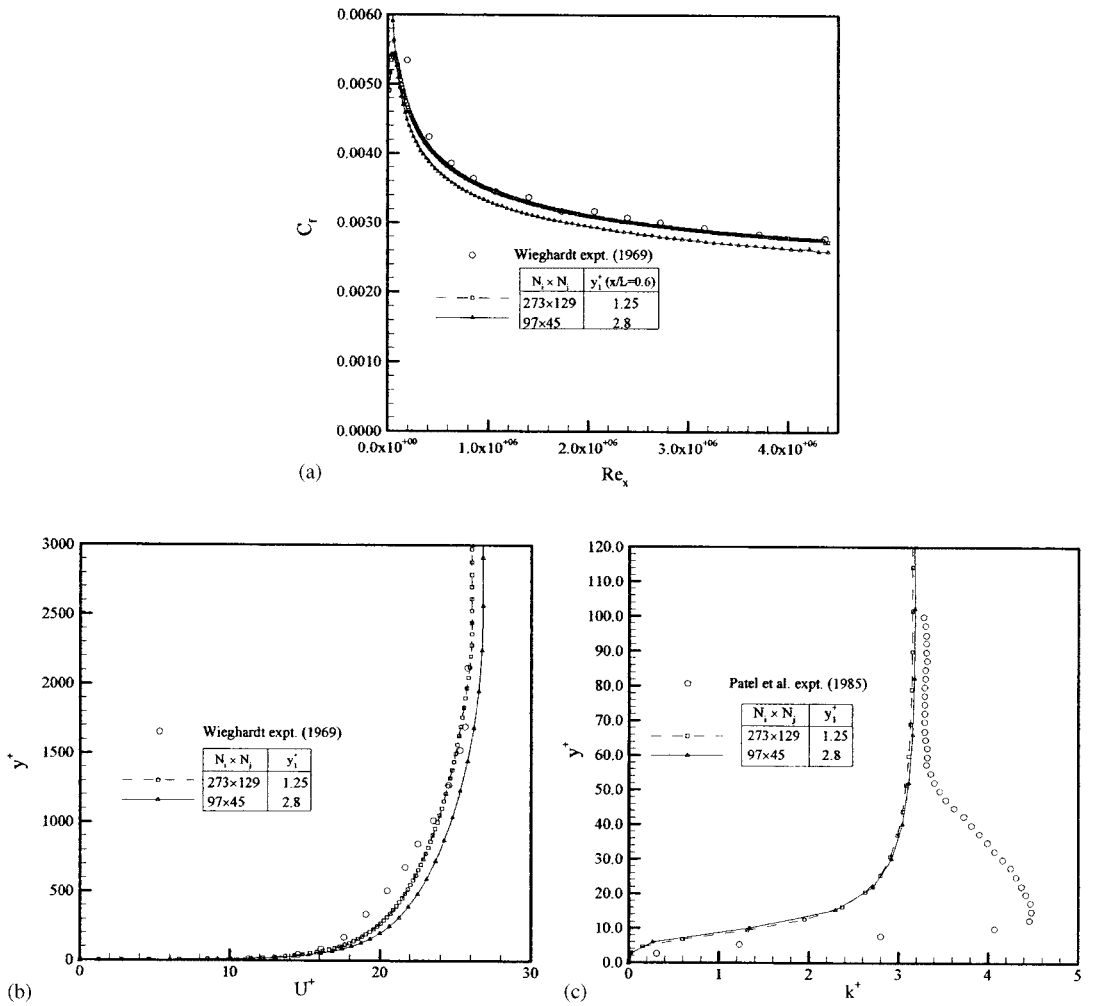

Figure 2. Flat-plate predictions based on the k–ω model—sensitivity to spatial resolution: (a) C_f distribution; (b) velocity profile at $(x/L, = 0.6)$; and (c) k profile at $(x/L = 0.6)$.

prediction accuracy to be very sensitive to changes in β_{wall}, with a value of 1.25 providing the best results.

3.3.3. Sensitivity to freestream turbulence parameters. Simulations based on Rodi's k–ε model with $k = 1.3 \times 10^{-3}$ and a range of ε values from 1 to 100 in the freestream resulted in essentially the same predictions of velocity and k distributions in the boundary layer. This observation is in agreement with suggested values of freestream μ_e in the published literature [8, 22].

For both the k–ω and SST turbulence models, freestream values of ω, k and μ_e were systematically adjusted within the ranges of: $\omega = 100$–5000; $k = 1.8 \times 10^{-6}$ to 1.8×10^{-3} and

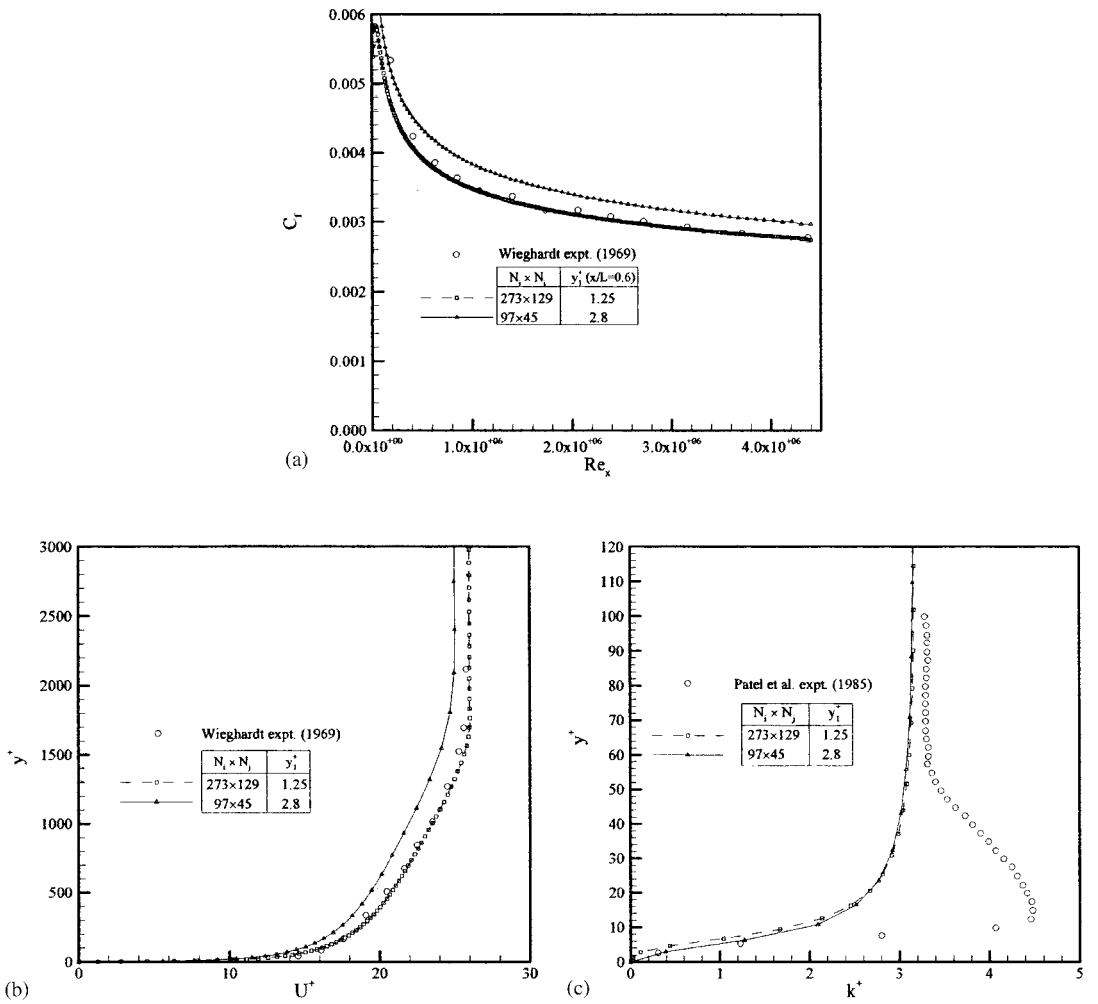

Figure 3. Flat-plate predictions based on Menter's SST model—sensitivity to spatial resolution: (a) C_f distribution; (b) velocity profile at $(x/L = 0.6)$; and (c) k profile at $(x/L = 0.6)$.

$\mu_e/\mu = 2 \times 10^{-4}$ to 1×10^{-1}. The only noticeable sensitivity was noted to be with respect to the value of ω, with a value of 100 appearing as the best choice for both turbulence models. For the values of 100, 1000 and 5000 that were considered, the k–ω model displayed notable sensitivity to a change in ω from 100 to 1000, whereas variations in the predictions were only evident between ω values of 1000 and 5000 with the SST model.

Finally, sensitivity of the predictions with the SA model to freestream eddy viscosity was examined through variations of $\chi = \tilde{\nu}_e/\nu$ from 0.24 to 1.4, which corresponds to a μ_e/μ range of 1×10^{-5} to 1×10^{-2}. The changes in the predicted velocity and C_f distributions were negligibly small.

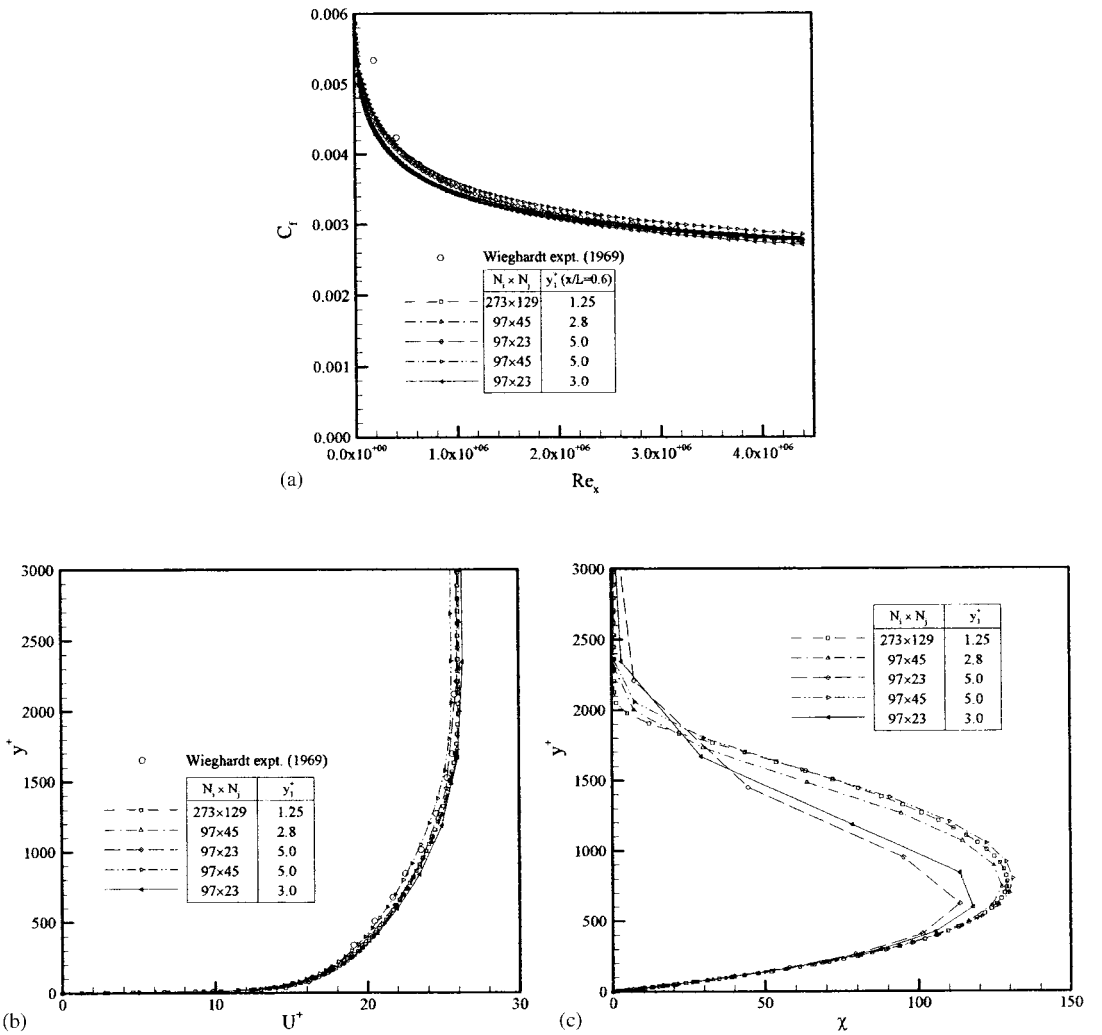

Figure 4. Flat-plate predictions based on the SA model—sensitivity to spatial resolution: (a) C_f distribution; (b) velocity profile at $(x/L = 0.6)$; and (c) χ profile at $(x/L = 0.6)$.

4. SIMULATIONS OF SEPARATING FLOW IN AN ANNULAR DIFFUSER

The axisymmetric, separating, adverse-pressure-gradient flow identified as Case C.S0 by Driver and Johnston [26] constituted the second test case of the present study. In this experiment, Driver and Johnston used an annular diffuser which was formed by aligning a cylinder longitudinally in a wind-tunnel test section with diverging walls. Boundary layer suction was applied at the test section walls such that separation occurred on the cylinder surface only. Prediction of the flow in this test case is particularly challenging since the separation bubble is not constrained in the axial direction.

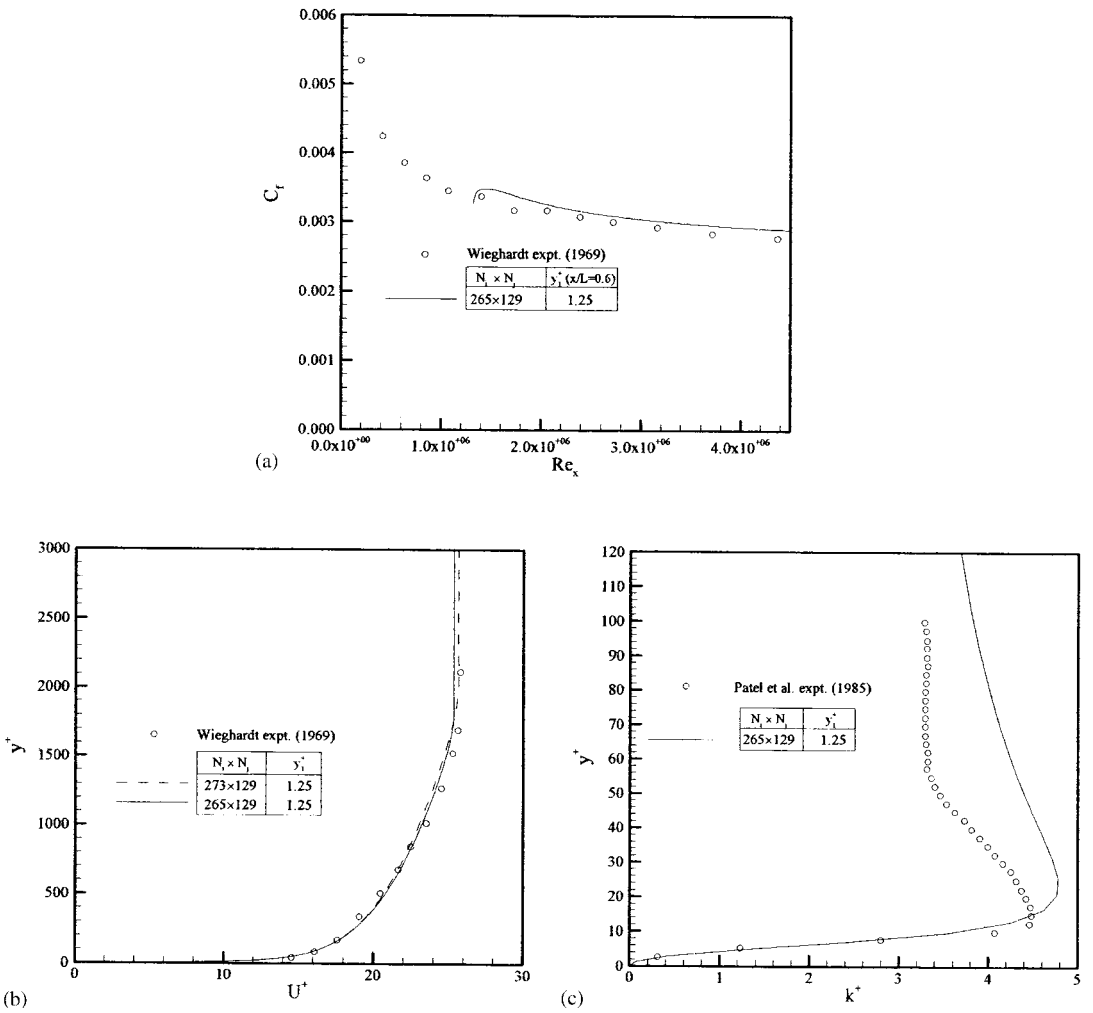

Figure 5. Flat-plate predictions based on Chien's k–ε model: (a) C_f distribution; (b) velocity profile at $(x/L = 0.6)$; and (c) k profile at $(x/L = 0.6)$.

4.1. Computational domain

The size of the computational domain was minimized by prescribing a domain boundary at the larger radius that followed a stream-surface rather than extending the domain to the test-section walls. The shape of this stream-tube was defined on the basis of mass conservation. Figure 6 gives a cross-sectional view of the resulting axisymmetric computational domain. The computational domain was selected to be 1.26 m long. The distance $(R_S - R_0)$ between the surface of the inner cylinder and the outer slip-boundary ranged from a minimum of 0.037 m at the inlet to a maximum of 0.071 m in the region of separation.

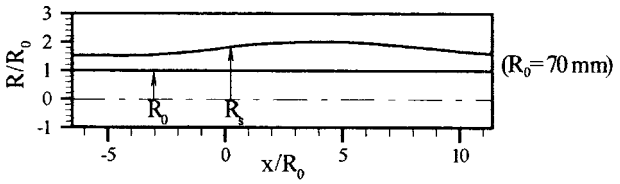

Figure 6. Computational domain used for Driver and Johnston's C.S0 test case.

4.2. Computational grid

Grid dependence tests revealed that a minimum of 15 nodes were required in the boundary layer for each of the four turbulence models. The maximum allowable value for y_1^+ was found to be 5.0 for the SA and Rodi's k–ε models, while it had to be reduced to 1.3 for the other models. These results are consistent with the observations in the flat-plate simulations. For consistency, comparison of the predictions with different turbulence models against experimental data was based on a single grid that exceeds the minimum requirements of the most stringent turbulence model. For this purpose, a conservative grid was designed consisting of 89 and 61 nodes in the streamwise and radial directions, respectively, with $y_1^+ = 1.28$ and about 40 nodes in the boundary layer at the inflow boundary. The variation of cross-stream clustering of the nodes with streamwise distance was chosen to ensure similar resolution of the boundary layer elsewhere.

4.3. Boundary conditions and iteration parameters

Profiles of velocity and turbulence quantities were specified at the inflow boundary. The experimental data corresponding to the location of the inflow boundary of the computational domain ($x = -0.457$ m) were found to agree well with the profiles of a simulated flat-plate boundary layer with the same Re_θ of 2760. Since the experimental profiles were relatively sparse, and not all of the turbulence quantities were part of the measured data set, the simulated flat-plate boundary layer data were used to specify the inflow boundary conditions. The freestream velocity at the inflow boundary was set to 30 m/s as per the experiments. The values used for the turbulence quantities in the freestream portion of the inflow boundary were: $k = 1.3 \times 10^{-3}$, $\varepsilon = 7$ for the k–ε models of Rodi and Chien; $k = 1.8 \times 10^{-6}$, $\omega = 100$ for the k–ω and SST models; and $\chi = 0.77$ for the SA model.

At the outflow boundary, the static pressure was set to a uniform value and all other flow properties were extrapolated from the interior of the computational domain. It is well known that fixing of static pressure at an outflow boundary results in reflection of transient waves that develop during pseudo-time marching. To reduce the extent of this reflection, the following boundary condition was used for the outflow pressure, the compressible-flow version of which was originally proposed by Rudy and Strikwerda [27]:

$$\frac{\partial P}{\partial t_p} - \rho a_s \frac{\partial V_{\mathrm{local}}}{\partial t_p} + \alpha_P (P - P_{\mathrm{BC}}) = 0 \tag{19}$$

where α_P is a constant set to 1/8 for the present test case, P_{BC} is the desired pressure value at the outflow boundary, and a_s, which is normally the speed of sound in a purely compressible

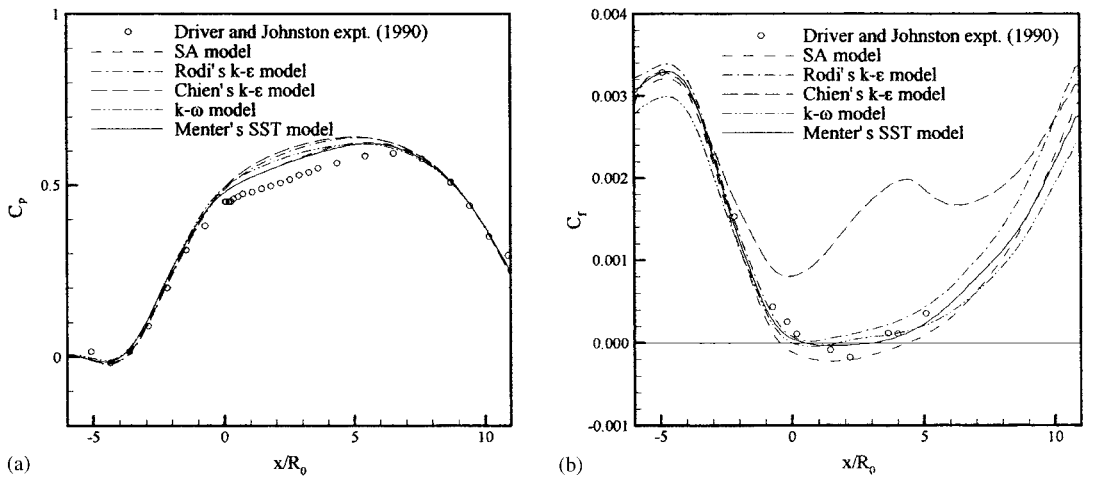

Figure 7. Comparison of predictions with Driver and Johnston's experimental data: (a) C_p distribution; and (b) C_f distribution.

flow solver, is evaluated as

$$a_s = \sqrt{(V_{\text{local}})^2 + (c/a)^2} \tag{20}$$

to reflect the preconditioned nature of the governing equations being solved by the present algorithm. Although the use of this less reflective outflow pressure boundary in the C.S0 test case substantially reduced the magnitude of the pressure oscillations during pseudo-time stepping, ultimate convergence to a solution was still not possible with two-grid-level multigrid cycles. After a sufficient number of multigrid cycles to develop the overall velocity and pressure fields, single-grid iterations were needed to complete the solution. These convergence difficulties encountered with this flow were absent in the simpler flat-plate test case, as well as the complex three-dimensional flows to be discussed in sections that follow. Separating flows in diffusing ducts, such as in the C.S0 test case, tend to be inherently unsteady. Even if a steady state is achieved in a well-controlled environment, which seems to be the case in Driver and Johnston's experiments, this state may easily be perturbed by small disturbances. The difficult-to-control transient behaviour observed numerically during pseudo-time stepping may be merely a reflection of this nature of the flow.

For optimum rates of convergence, the artificial compressibility parameter, c/a, was set to $\max[10.0\ \text{m/s};\ 1.0\ V_{\text{local}}]$, while the convective and diffusive time-step limits were determined on the basis of $K_c = 1.8$, $K_d = 0.1$. The artificial dissipation parameter, κ_4, was set to 0.005 as per the flat plate simulations. Initial and lower threshold settings of the turbulence parameters k, ε, ω and χ, were the same as those used in the flat plate simulations.

4.4. Simulation results

As noted in Figure 7(a), all models reproduce the correct pressure distributions upstream and downstream of the separation bubble. The SA and SST models more accurately capture the

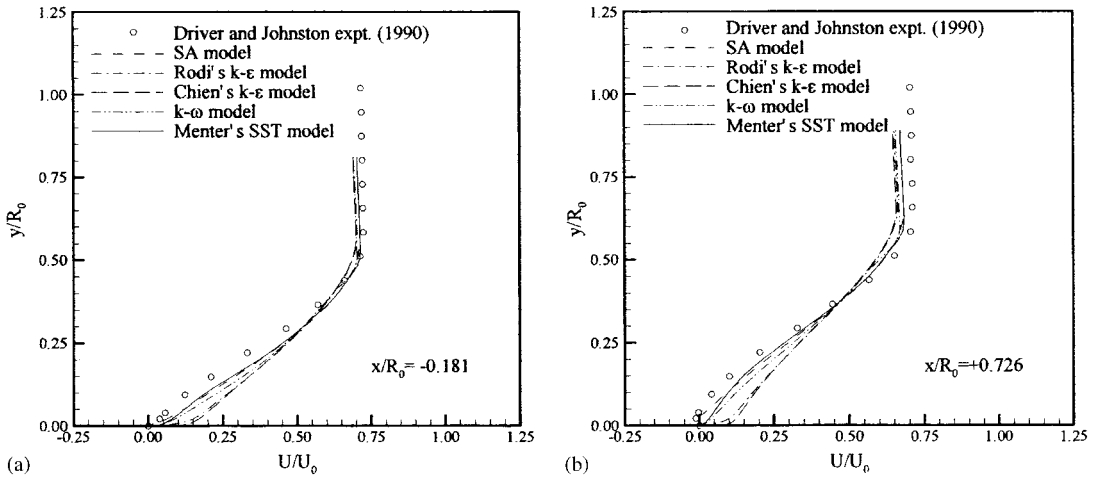

Figure 8. Comparison of predicted velocity profiles with Driver and Johnston's experimental data: (a) $x/R_0 = -0.181$; and (b) $x/R_0 = 0.726$.

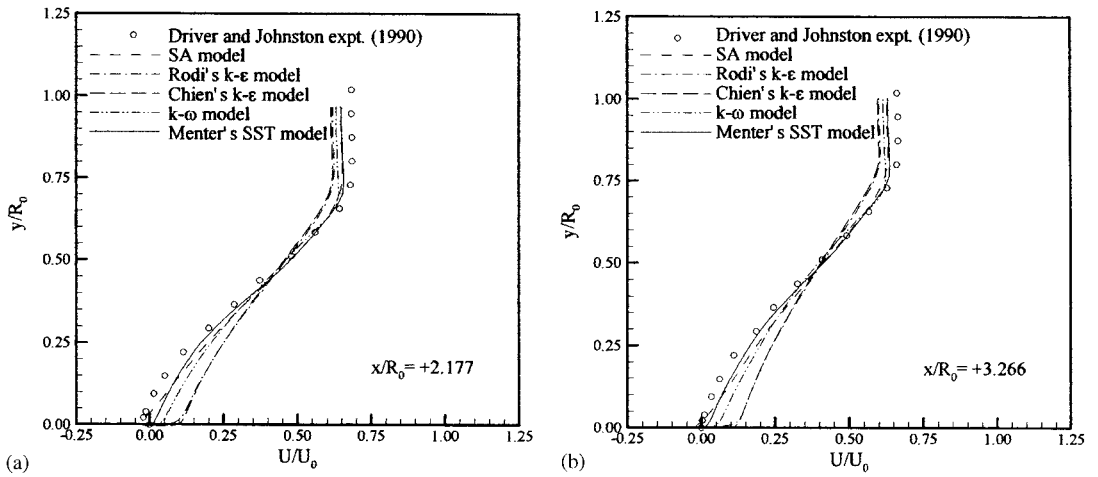

Figure 9. Comparison of predicted velocity profiles with Driver and Johnston's experimental data: (a) $x/R_0 = 2.177$; and (b) $x/R_0 = 3.266$.

flat portion of the C_p curve in the separated region. However, calculations with all models result in over-prediction of static pressure in the region of separation. Predictions of C_f are shown in Figure 7(b). Separation is not predicted by Chien's k–ε model at all, and no flow reversal is captured by Rodi's k–ε model. The poor prediction of C_f by Chien's model was found to be related to periodic variations of streamwise velocity along the length of the domain which prevailed along the first three grid lines next to the wall. Reduction of y_1^+ to 0.25 did not solve this problem. Similar C_f trends have been observed by Dudek *et al.* [28] and Shih [29], which suggests that this may be a fundamental deficiency of Chien's k–ε

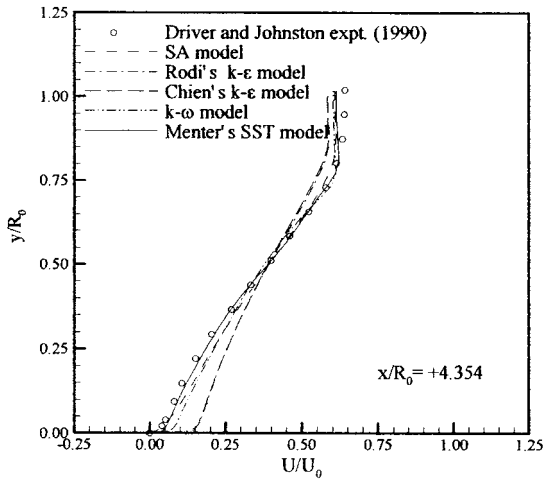

Figure 10. Comparison of predicted velocity profiles with Driver and Johnston's experimental data ($x/R_0 = 4.354$).

Table I. Predicted separation and reattachment points compared with Driver and Johnston's experimental data.

Location	Experiment	SA	Rodi's k–ε	k–ω	SST
Separation (x/R_0)	0.6	−0.5	0.5	0	0.5
Re-attachment (x/R_0)	3.2	4.4	0.5	1.7	3.1

formulation. Due to this problem, and the requirement of limiting the turbulence production rate even for a flat-plate flow, Chien's k–ε model was excluded from the remainder of this study. As presented in Figures 8–10, Menter's SST model is most successful in capturing the trends in the velocity field followed by the SA and k–ω models. Locations of separation and reattachment, summarized in Table I, are also most accurately predicted by the SST model. Predictions of k profiles, shown in Figures 11–13, indicate a common trend for all models to underestimate the peak value. This trend is consistent with the results obtained for the flat plate boundary layer.

5. SIMULATIONS OF A CONFINED SWIRLING FLOW

The third test case was based on the experimental data of So *et al.* [30]. The flow consists of an annular swirling stream introduced into a circular pipe of $D = 0.125$ m diameter in conjunction with a non-swirling concentric jet of $D_j = 0.00873$ m diameter. The swirl number,

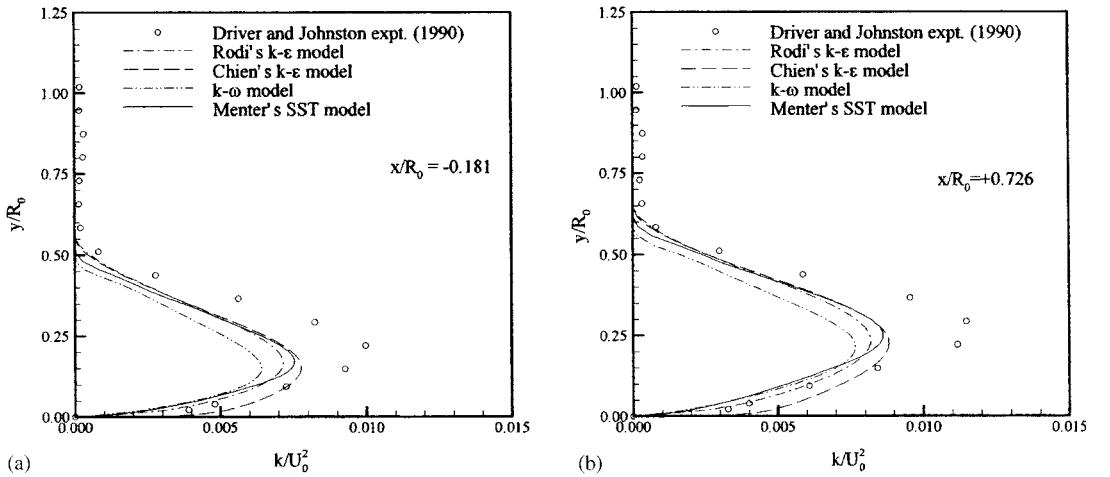

Figure 11. Comparison of predicted k profiles with Driver and Johnston's experimental data: (a) $x/R_0 = -0.181$; and (b) $x/R_0 = 0.726$.

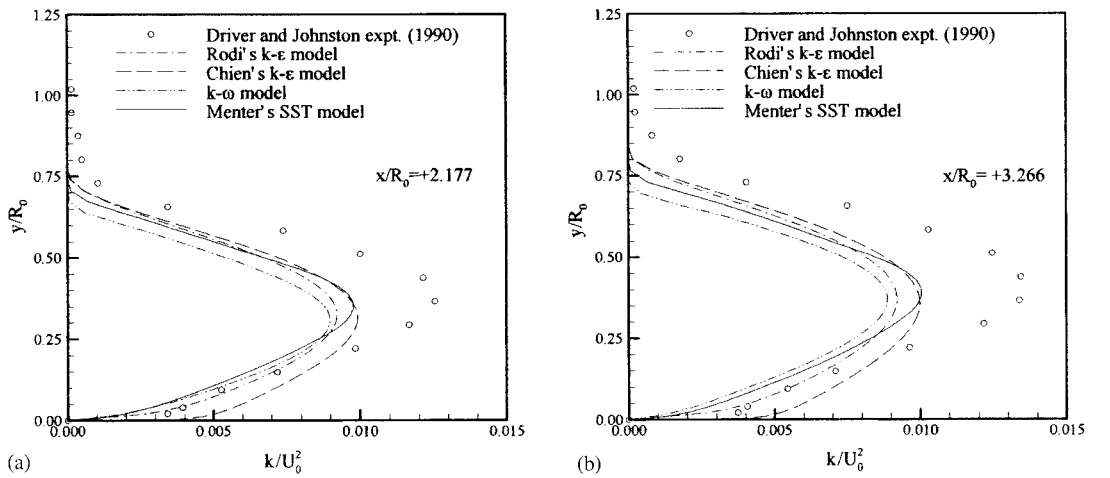

Figure 12. Comparison of predicted k profiles with Driver and Johnston's experimental data: (a) $x/R_0 = 2.177$; and (b) $x/R_0 = 3.266$.

S, defined as

$$S = \frac{\int_0^{D/2} V_x V_t r^2 \, \mathrm{d}r}{(D/2)\int_0^{D/2} V_x^2 r \, \mathrm{d}r} \tag{21}$$

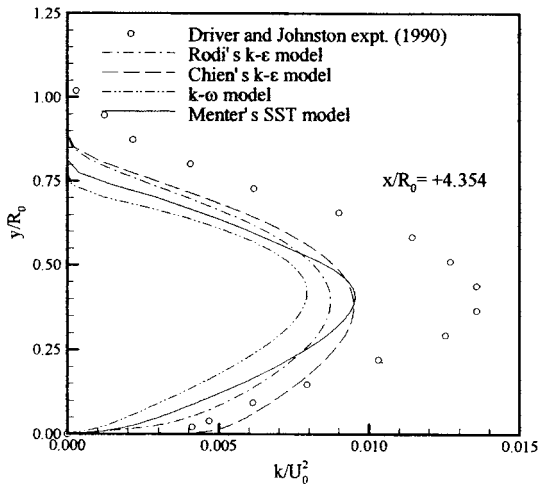

Figure 13. Comparison of predicted k profiles with Driver and Johnston's experimental data ($x/R_0 = 4.354$).

was close to 2.25 just downstream of the swirl generator, which is indicative of a strongly swirling flow. The authors considered several variations of core-jet velocity and jet-to-swirl ing flow density ratios. For the present simulations, the data set corresponding to a core jet velocity of $V_j = 25.4$ m/s and a density ratio of 1.0 was used. In this instance, the core-jet Reynolds number based on D_j and V_j was 1.44×10^4. A laser-Doppler anemometer was used to measure the axial and circumferential velocity components. Since the radial component of velocity was not measured, it is not possible to establish the prediction accuracy of k with the present turbulence models without making assumptions about the isotropy of the turbulence field. The comparisons for this test case will therefore be limited to the mean velocity field.

5.1. Computational domain, boundary conditions and iteration parameters

Measurements were conducted by So *et al.* at several streamwise positions up to $40D_j$ downstream of the swirl-generating vanes. The computational domain was therefore selected to be $45D_j$ long, with the inflow boundary placed at $1.0D_j$ away from the plane of the swirl generator, coinciding with the most upstream location for which measurements were available. At the inflow boundary, the velocity magnitude and direction were specified as per the measurements. The turbulence kinetic energy was determined from the measured Reynolds normal stresses assuming the radial and circumferential normal stresses to be the same, since the former quantity was not available. Radial distributions of axial and tangential mean velocity components as well as k are shown in Figure 14. The solid curves indicate the polynomial fits that were used to represent the inflow conditions for the computations.

In absence of experimental data for ε, this quantity was determined using

$$\varepsilon = \frac{k^{3/2}}{0.2D_h} \tag{22}$$

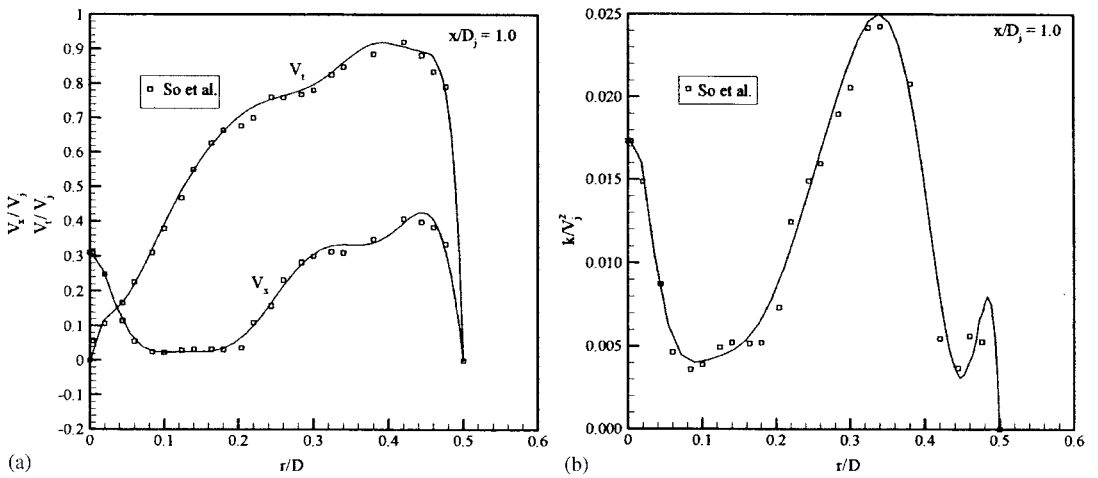

Figure 14. Distributions of: (a) V_x, V_t; and (b) k at $x/D_j = 1$.

where D_h is the hydraulic diameter. This approach of evaluating ε is common [31]. Various methods for estimating ε in jet flows were evaluated by Nikjoo and Mongia [32], who found Equation (22) to perform equally well as more elaborate alternatives. Upon establishing the ε distributions, determining the ω and $\tilde{\chi}$ distributions for use with the k–ω, SST and SA turbulence models is straight forward.

At the outflow boundary the static pressure was fixed at one node. The cross-stream pressure gradients and all other flow properties were extrapolated from the interior of the domain. Simulations with a longer computational domain ($90D_j$) confirmed that such treatment of the outflow boundary did not have a non-physical influence at the most downstream position where the predictions are compared to measurements ($40D_j$). In instances where the maximum swirl velocity exceeds the average axial velocity, such is the case in the present flow, a subcritical state is reached in which the flow tends to be highly sensitive to downstream disturbances [33–35]. Chen and Lin [35], who simulated the flow of So *et al.* as well, opted to prescribe the axial velocity at the outflow boundary to circumvent this problem. In the present simulations, such over-specification of the outflow boundary conditions was not used, albeit at the expense of significantly reduced convergence rates.

For optimum rates of convergence, the artificial compressibility parameter, c/a, was set to $\max[20.0\ \mathrm{m/s}; 3.2V_{\mathrm{local}}]$, while the convective and diffusive time-step limits were determined on the basis of $K_c = 1.8, K_d = 0.1$. The artificial dissipation parameter, κ_4, was set to 0.005 as per the flat-plate and annular diffuser flows. Initial and lower threshold settings of the turbulence parameters k, ε, ω and χ, were also the same as those used in these previous test cases.

5.2. Computational grid

In mapping a structured grid consisting of hexahedral elements onto a circular geometry, relatively significant skewing of the elements is difficult to avoid. This is clearly evident in Figure 15(a) where substantial distortion of the elements is noted at four locations along the

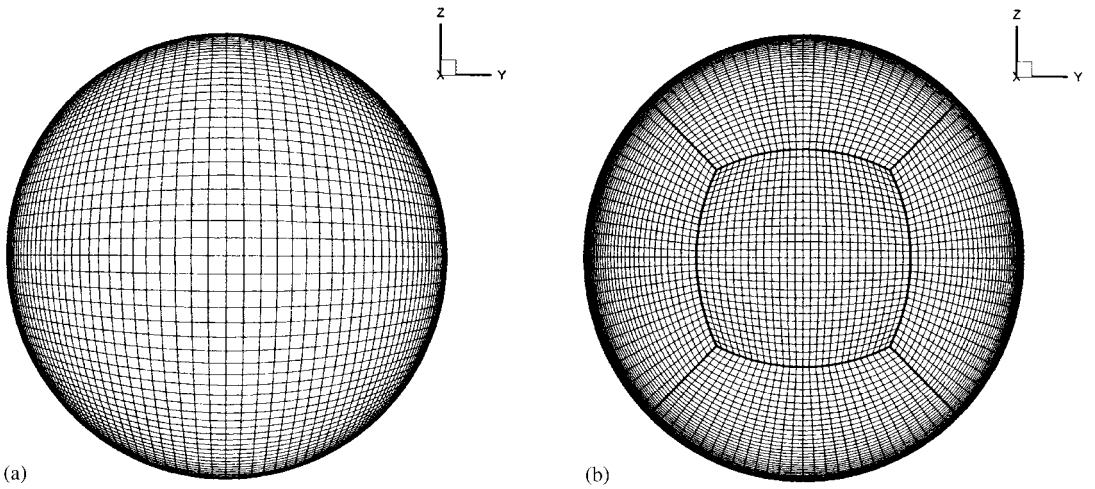

Figure 15. Computational grid in the cross-sectional plane for the confined swirling flow: (a) single-block grid; and (b) multi-block grid.

circumference of the circular cross section. Such skew may have both convergence and accuracy implications. An effective way to circumvent this problem while retaining the hexahedral-structured characteristics of the grid is to use a multi-block structured grid, as shown in Figure 15(b). The simulation results to be presented here were based on this multi-block grid configuration. The grid is divided into five blocks in the cross-sectional plane, with four even-sized blocks surrounding a central block. In each of the four blocks surrounding the central block, 41 and 29 nodes were used in the radial and circumferential directions, respectively. The central block was discretized by 29 nodes in the two cross-stream grid directions. Radial clustering of the nodes in the outer blocks was such that the number of nodes in the wall boundary layer and the y^+ value of the first node off the wall met the minimum requirements of the most stringent turbulence model as per the flat-plate and annular diffuser test cases. In the axial direction, 61 nodes were used in each block, and the nodes were distributed evenly in light of the relatively low streamwise gradients in velocity and pressure prevailing in this flow.

A multi-block grid is clearly quite effective in adapting to complex geometries, and in optimizing the node distribution. However, one ought to expect a reduction in the stability bounds of an implicit algorithm when used on such a grid, since pseudo-time iterations take place explicitly at the block level. For this reason, and for the relative simplicity of grid generation, a single-block grid may be desirable in an industrial setting where turn-around time is often equally important as accuracy. Selective simulations were performed with the single-block grid configuration shown in Figure 15(a) to investigate the impact of increased grid skewness on accuracy and numerical stability. The grid contained 73 nodes in each of the cross-stream grid directions and 61 nodes in the axial direction. The proximity of the nodes adjacent to the duct wall is clearly not circumferentially uniform in this instance. Radial clustering of nodes was set such that the largest y_1^+ remained within the range required by the turbulence models in question. Simulations based on this computational grid did not converge

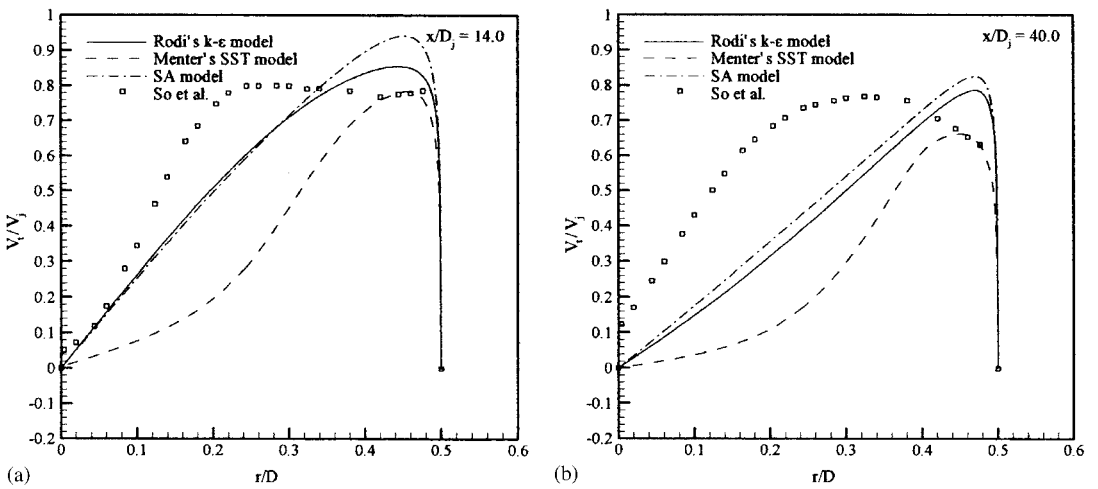

Figure 16. Radial distributions of the tangential velocity component: (a) $x/D_j = 14$; and (b) $x/D_j = 40$.

to a solution due to numerical difficulties arising from the nearly collapsed cells located at the four "corners" of the grid along the duct wall. Excluding 8×8 blocks of nodes at these locations from the computations resolved this problem. Deviation from a circular cross-section caused by the exclusion of these cells from the computational domain was less than 0.1% of the duct radius. Furthermore, this approach facilitated a more uniform distribution of y_1^+ along the duct wall. The predicted flow field with the grid was essentially the same as that based on the multi-block grid, except for very slight thickening of the boundary layer on the duct wall at the four "corners" of the grid. Thus, at least with the spatial discretization utilized by the present algorithm, such skewed grids may be used with little penalty in prediction accuracy.

5.3. Simulation results

The primary purpose of this test case was to examine the capabilities of the turbulence models in capturing the effect of streamline curvature on the local turbulence. In absence of measurements for the turbulence quantities used by the models, examination of the radial redistribution of angular momentum with streamwise distance, as shown in Figure 16, is deemed most effective in revealing the accuracy of the turbulence models in this respect.

All turbulence models are noted to yield excessive radial diffusive transport. In the case of the k–ε and SA models, the prediction accuracy is similar, and the flow assumes a solid body rotation at a rate significantly higher than the measurements. In comparison, the SST model is noted to yield very poor predictions of this tangential velocity field. It was not possible to converge the k–ω model to a solution without imposing upper limits on the eddy viscosity and the production-to-dissipation ratio of turbulence. These limits had to be set to such low values that they interfered with the natural development of the k and μ_ε fields. Hence, the results for this turbulence model were deemed unreliable in this test case.

In an attempt to increase the prediction accuracy of the turbulence models, corrections for streamline curvature included in the turbulence transport equations as described earlier

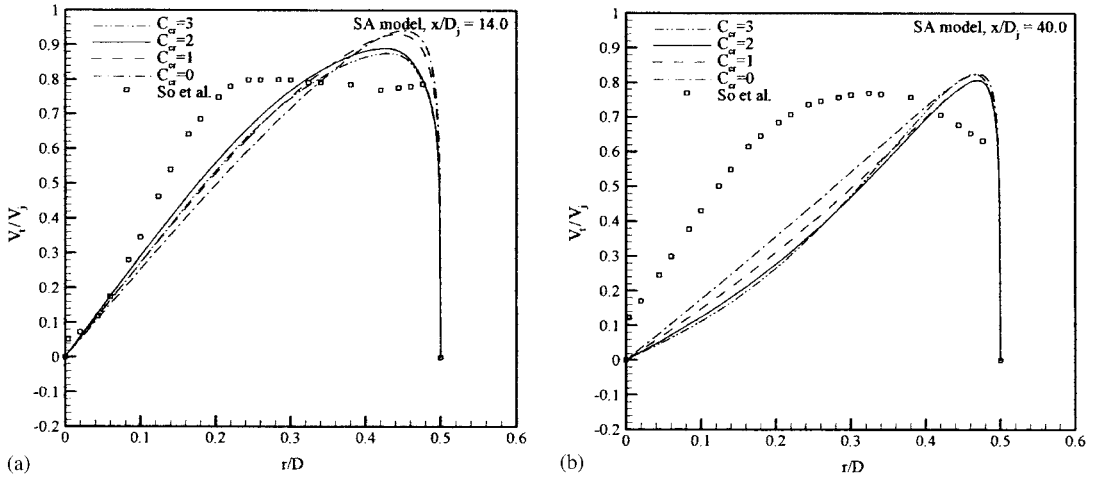

Figure 17. Effects of curvature correction on the tangential velocity field: (a) $x/D_j = 14$; and (b) $x/D_j = 40$.

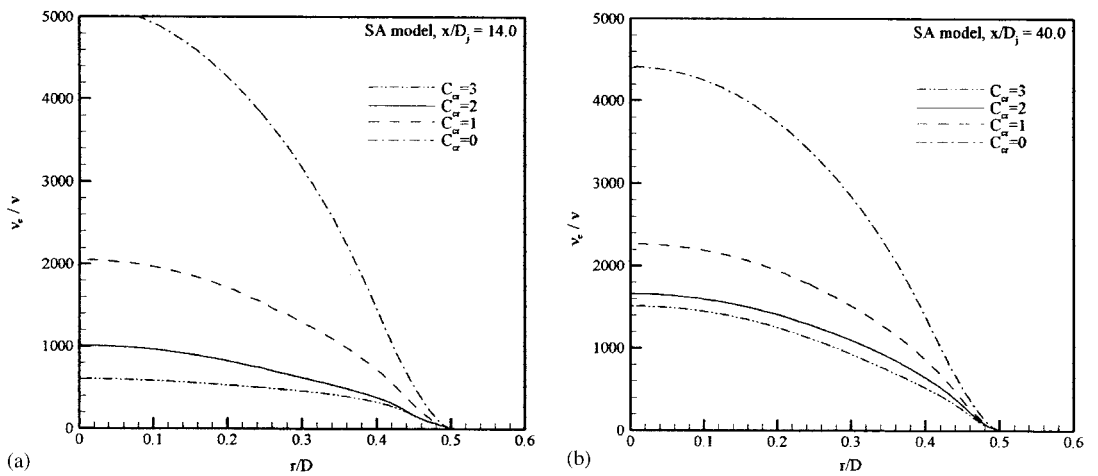

Figure 18. Effects of curvature correction on the radial eddy viscosity distribution: (a) $x/D_j = 14$; and (b) $x/D_j = 40$.

(Equation (14)), The results for the SA model with a series of values of the curvature/rotation coefficient, C_{cr}, within its applicable range are shown in Figure 17. A noteworthy improvement is not evident in the tangential velocity distribution. Introduction of the curvature correction does in fact reduce the eddy viscosity substantially, as shown in Figure 18. However, since the radial variation of tangential velocity is linear over a large portion of the duct radius, the reduction in the eddy viscosity does not affect the tangential velocity field to a significant extent. Similarly disappointing results were obtained with the SST and k–ε models. In absence

of confirmed benefits of such curvature corrections, they were not used in the simulations of the three-dimensional flows that follow in Part II of this study.

6. CONCLUSIONS

In this segment of the two-part study, the low-Re k–ε model of Chien [5], the two-layer k–ε model of Rodi [6], the k–ω model of Wilcox [7], the two-equation shear-stress-transport model of Menter [8], and the one-equation eddy-viscosity model of Spalart and Allmaras [9] were evaluated for prediction accuracy, numerical robustness and computational efficiency. None of the models were based on wall-function boundary conditions, and the following main conclusions are drawn based on comparison with experimental results for three flows:

- All turbulence models were found to provide satisfactory development of the boundary layer over a flat plate in terms of velocity and wall shear stress distributions. Only Chien's k–ε model was able to reproduce the trends in the profile for turbulence kinetic energy, albeit only qualitatively.
- All but Chien's k–ε model were fairly successful in capturing the surface pressure and skin friction distributions in an axisymmetric separating flow. A slight overprediction of the static pressure in the separated zone was common for the models. Menter's SST model was the most successful in capturing the trends in the velocity profiles followed by the SA and k–ω models; Rodi's k–ε model performed rather poorly in this respect. Those models that solve for the turbulence kinetic energy, k, failed to capture the peak k value in the boundary layer, which is consistent with the observations in the flat plate boundary layer.
- In terms of minimum grid resolution requirements for both the flat plate and the axisymmetric separating flows, Rodi's k–ε and the SA models showed the best performance, requiring a maximum of $y_1^+ = 5$ and at least 15 nodes within the boundary layer for acceptable prediction accuracy. The required minimum node count was about the same for the k–ω and SST models, whereas the upper limit for y_1^+ had to be set at about 1.3 for comparable accuracy.
- The prediction of a strongly swirling confined flow was rather poor, with all tested models (Rodi's k–ε, SST and SA models) significantly overestimating the radial diffusive transport. Amongst these models, the SST model yielded the worst prediction. Use of streamline-curvature corrections in the turbulence transport equations had little impact on the prediction accuracy.

NOMENCLATURE

$a_1 \ldots a_4$	constants used in scaling the preconditioning parameter, c
a_s	a parameter used in outflow boundary specification of pressure
c	parameter used in the preconditioning of Q in the $\partial Q/\partial t_p$ term
C_f	skin friction coefficient $(= \tau_w/(1/2\rho_{\text{ref}} V_{\text{ref}}^2))$
C_{cr}	constant used in F_{cr}
C_p	static pressure coefficient

D	artificial dissipation operator; pipe diameter
D_j	jet diameter
D_h	hydraulic diameter
E, F, G	convective+diffusive flux vectors in the x, y and z directions, respectively
F_{cr}	curvature/rotation correction function used in the turbulence models
i, j, k	node indices in the ξ, η, ζ grid directions
K_c, K_d	constants used in determining the convective and diffusive pseudo-time-step limits
k	turbulence kinetic energy ($\mathrm{m}^2/\mathrm{s}^2$)
k_R^+	wall-roughness height normalized by ν/U,
L	length of flat plate
n	direction normal to a wall
N_i, N_j, N_k	number of nodes in the i, j, and k grid directions, respectively
P	pressure
P_{BC}	static pressure fixed at an outflow boundary
Q	vector of conservation variables
r, R	radial co-ordinate
R_0	hub radius in Driver and Johnston's annular-flow test section ($= 70\,\mathrm{mm}$)
R_s	radius of the streamline forming the 'outer' boundary of the computational domain in Driver and Johnston's C.S0 test case
Re	Reynolds number
Re_θ	Reynolds number based on the boundary layer momentum thickness
S	surface area of control volume; swirl number; scalar measure of local strain-rate tensor ($= \sqrt{2S_{ij}S_{ij}}$)
S_{ij}	strain-rate tensor
S_R	function used in obtaining wall value of ω in the k–ω model
t	time
t_p	pseudo-time
U	x-velocity component
U_τ	friction velocity ($= (\tau_w/\rho)^{1/2}$)
U^+	streamwise velocity normalized by U_τ
V	velocity vector; y-velocity component
V_j	jet velocity (m/s)
V_{local}	local velocity magnitude (m/s)
V_t	cross-stream (tangential) velocity component
V_x	x-velocity component
V_y	y-velocity component
V_z	z-velocity component
x, y, z	cartesian co-ordinates
y_1	perpendicular distance from wall to first grid node off the wall
$\kappa^{(2)}, \kappa^{(4)}$	constants used in the calculation of artificial dissipation
α_p	coefficient used in outflow pressure specification
β_{wall}	coefficient used for ω_{wall} calculation in Menter's SST turbulence model
δ	boundary layer thickness
Δt_c	convective pseudo-time-step limit
Δt_d	diffusive pseudo-time-step limit

λ	spectral radius of the inviscid flux Jacobian
ν	kinematic viscosity
ν_e	kinematic turbulence (eddy) viscosity
$\tilde{\nu}_e$	eddy-viscosity variable used in the Spalart–Allmaras turbulence model $= \nu_e(\chi^3 + 7.1^3)/\chi^3$
μ	dynamic viscosity
μ_e	dynamic eddy viscosity
χ	$\dfrac{\tilde{\nu}_e}{\nu}$
ρ	density
τ	viscous + Reynolds stress
τ_w	wall shear stress
Ω	magnitude of vorticity
ξ, η, ζ	co-ordinates aligned with grid directions on a structured grid
ε	dissipation rate of turbulence kinetic energy (m^2/s^3)
$\varepsilon^{(2)}, \varepsilon^{(4)}$	scaling parameters used in the calculation of artificial dissipation
$\tilde{\varepsilon}$	modified turbulence dissipation rate used in Chien's low-Re k–ε model
ω	specific dissipation rate of turbulence kinetic energy (1/s)
ϑ	size of control volume

Subscripts

ref	reference quantities used for non-dimensionalization
wall	value on the wall

ACKNOWLEDGEMENTS

The research presented herein was undertaken with the financial support of National Research Council of Canada under contract no. 31184-8-8847/001/ST.

REFERENCES

1. Iacovides H, Launder BE. The numerical simulation of flow and heat transfer in tubes in orthogonal-mode rotation. In *Proceedings of the 6th Symposium on Turbulent Shear Flows*, 1987.
2. Patel VC, Rodi W, Scheuerer G. Turbulence models for near-wall and low-Reynolds-number flows: a review. *AIAA Journal* 1985; **23**:1308–1319.
3. Shih TH, Mansour NN. Modelling near-wall turbulence. In *Engineering Turbulence Modelling and Experiments*, Rodi W, Ganic EN (eds). Elsevier: Amsterdam, 1990; 13–22.
4. Rodi W. Experience with two-layer models combining the k–ε model with a one equation model near the wall. *AIAA Paper 91-0216*; 1991.
5. Chien K-Y. Prediction of channel and boundary layer flows with a low-Reynolds-number turbulence model. *AIAA Journal* 1982; **20**:33–38.
6. Rodi W. Recent developments in turbulence modeling. In *Proceedings of the 3rd International Symposium on Refined Flow Modeling and Turbulence Measurements*, Iwasa Y, Tamai N, Wada A (eds). Tokyo, Japan, 1988.
7. Wilcox DC. *Turbulence Modeling for CFD* (2nd edn). DCW Industries, La Cañada, CA 1988.
8. Menter FR. Eddy viscosity transport models and their relation to the k–ε model. *NASA Technical Memorandum TM-108854*, 1994.
9. Spalart PR, Allmaras, SR. A one equation turbulence model for aerodynamic flows. *AIAA Paper 92-0439*, 1992.
10. Crumpton PI, Shaw GJ. A vertex-centered finite volume method with shock detection. *International Journal for Numerical Methods in Fluids* 1994; **18**:605–625.

11. Jameson A, Schmidt W, Turkel E. Numerical solutions of the Euler equations by finite volume methods using Runge–Kutta time-stepping schemes. *AIAA Paper 81-1259*, 1981.
12. Swanson RC, Turkel E. Artificial dissipation and central difference schemes for the Euler and Navier–Stokes equations. *AIAA Paper 87-1107*, 1987.
13. Turkel E, Vatsa VN. Effect of artificial viscosity on three-dimensional flow solutions. *AIAA Journal* 1994; **32**:39–45.
14. Lin FB, Sotiropoulos F. Assessment of artificial dissipation models for three dimensional incompressible flow solutions. *Journal of Fluids Engineering* 1997; **119**:331–340.
15. Turkel E. Preconditioned methods for solving the incompressible and low speed compressible equations. *Journal of Computational Physics* 1987; **72**:277–298.
16. Stone HL. Iterative solution of implicit approximation of multidimensional partial differential equations. *SIAM Journal of Numerical Analysis* 1968; **5**:530–558.
17. Schneider GE, Zedan M. A modified strongly implicit procedure for the numerical solution of field problems. *Journal of Numerical Heat Transfer* 1981; **4**:1–19.
18. Brandt A. Multi-level adaptive solutions to boundary value problems. *Mathematics of Computation* 1977; **31**:333–390.
19. Yaras MI, Grosvenor AD. Numerical simulations of diffusing S-duct and vortex-generator-jet flows. *National Research Council of Canada Contract Report no. 31184-8-8847/001/ST*, 2000.
20. Hellsten A. Some improvements in Menter's k–ω SST turbulence model. *AIAA Paper 98-2554*, 1998.
21. Hellsten A. On the solid-wall boundary condition of ω in the k-ω-type turbulence models. *Report No B-50, Series B. Helsinki University of Technology*, *Finland*, 1998.
22. Bardina JE, Huang PG, Coakley TJ. Turbulence modeling validation, testing, and development. *NASA TM-110446*, 1997.
23. Heidegger NJ, Hall EJ, Delaney RA. Follow-on low noise fan aerodynamic study. *NASA CR-1999-206599*, 1999.
24. Wieghardt K, Tillmann W, Wieghardt. Flat plate flow. In *Computation of Turbulent Boundary Layers*, *Proceedings of AFOSR-IFP Stanford Conference 1968*, *Stanford University*, 1969; 98–123.
25. Patel VC, Rodi W, Scheuerer G. Turbulence models for near-wall and low-Reynolds number flows: a review. *AIAA Journal* 1985; **23**:1308–1319.
26. Driver DM, Johnston JP. Experimental study of a three-dimensional shear-driven turbulent boundary layer with streamwise adverse pressure gradient. *NASA TM 102211*, 1990.
27. Rudy DH, Strikwerda JC. A nonreflecting outflow boundary condition for subsonic Navier–Stokes calculations. *Journal of Computational Physics* 1980; **36**:55–70.
28. Dudek JC, Georgiadis NJ, Yoder DA. Calculation of turbulent subsonic diffuser flows using NPARC Navier–Stokes code. *AIAA Paper 96-0497*, 1996.
29. Shih T-H. Turbulence modeling developments at ICOMP. *AIAA Paper 98-3243*, 1998.
30. So RMC, Ahmed SA, Mongia HC. An experimental investigation of gas jets in confined swirling air flow. *NASA CR 3832*, 1984.
31. Henry FS, Pearcey HH. Numerical model of boundary-layer control using air-jet generated vortices. *AIAA Journal* 1994; **32**:2415–2425.
32. Nikjoo M, Mongia H. Study of non-linear k–ε model for turbulent swirling flows. *AIAA Paper 98-3984*, 1998.
33. Squire HB. Analysis of the vortex breakdown phenomenon. *Miszellanen der Angewandten Mechanik*, 1962; 306–312.
34. Escudier MP, Keller J. Recirculation in swirling flow: a manifestation of vortex breakdown. *AIAA Journal* 1985; **23**:111–116.
35. Chen JC, Lin CA. Computations of strongly swirling flows with second moment closures. *International Journal for Numerical Methods in Fluids* 1999; **30**:494–508.

